

Journal of Biomedical Optics

SPIEDigitalLibrary.org/jbo

Analysis of optimum conditions of depolarization imaging by polarization-sensitive optical coherence tomography in the human retina

Mitsuro Sugita
Michael Pircher
Stefan Zotter
Bernhard Baumann
Kenichi Saito
Tomoyuki Makihira
Nobuhiro Tomatsu
Makoto Sato
Christoph K. Hitzenberger

Analysis of optimum conditions of depolarization imaging by polarization-sensitive optical coherence tomography in the human retina

Mitsuro Sugita,^{a,b,*} Michael Pircher,^a Stefan Zotter,^a Bernhard Baumann,^a Kenichi Saito,^b Tomoyuki Makihira,^b Nobuhiro Tomatsu,^b Makoto Sato,^b and Christoph K. Hitzenberger^a

^aMedical University of Vienna, Center for Medical Physics and Biomedical Engineering, Waehringer, Guertel 18-20, Vienna A-1090, Austria

^bCanon Inc., 3-30-2 Shimomaruko, Ohta-ku, Tokyo 146-8501, Japan

Abstract. Measurement and imaging of depolarization by polarization-sensitive optical coherence tomography (PS-OCT) requires averaging of Stokes vector elements within two- or three-dimensional (3-D) evaluation windows to obtain the degree of polarization uniformity (DOPU). By use of a PS-OCT system with an integrated retinal tracker, we analyze optimum conditions for depolarization imaging, data processing, and segmentation of depolarizing tissue in the human retina. The trade-offs between figures of merit like DOPU imaging sensitivity, efficiency, and susceptibility are evaluated in terms of 3-D resolution. The results are used for a new, detailed interpretation of PS-OCT high-resolution images of the human retinal pigment epithelium and Bruch's membrane. © The Authors. Published by SPIE under a Creative Commons Attribution 3.0 Unported License. Distribution or reproduction of this work in whole or in part requires full attribution of the original publication, including its DOI. [DOI: [10.1117/1.JBO.20.1.016011](https://doi.org/10.1117/1.JBO.20.1.016011)]

Keywords: optical coherence tomography; retina; polarization; multiple scattering; image segmentation; ophthalmology.

Paper 140589RR received Sep. 14, 2014; accepted for publication Dec. 17, 2014; published online Jan. 13, 2015.

1 Introduction

Polarization-sensitive optical coherence tomography (PS-OCT) is a functional extension of OCT that has attracted considerable interest both from a research and an applications perspective.¹⁻¹¹

Ophthalmic applications are among the most successful fields of OCT,¹² and the tissue-specific contrast and quantitative information provided by PS-OCT led to several studies in healthy and diseased eyes.¹³⁻²¹ Biological tissues and structures of interest in ophthalmic applications are, e.g., the birefringent retinal nerve fiber layer (RNFL) and nerve fiber bundles for glaucoma diagnosis,^{13,22-24} and the depolarizing retinal pigment epithelium (RPE), which plays a decisive role in macular diseases, including age-related macular degeneration.

To quantify depolarization, we introduced a new parameter, the degree of polarization uniformity (DOPU), that is formally equivalent to the well-known degree of polarization (DOP), which cannot directly be measured by a coherent imaging technique like OCT. DOPU can be regarded as an averaged DOP and was used to segment depolarizing tissue like RPE¹⁶ and hard exudates,²⁵ as well as various lesions in macular disorders.²⁵⁻³⁰ According to our first introduction of the parameter, DOPU is calculated from a two-dimensional (2-D) PS-OCT B-scan frame via the Stokes vectors obtained at each pixel from amplitudes and the relative phase detected by the two orthogonal polarizations, and using a 2-D sliding average window (DOPU evaluation window for averaging the Stokes vectors) in (x, z) , where the xz -plane is parallel to the B-scan frame, and x and z denote scanning and depth directions, respectively.¹⁶ A typical window size is configured to be, for example, $8(x) \times 10(z)$ pixels in order to contain a sufficient number of (e.g., 80) Stokes

vectors to provide statistically relevant results for DOPU. The rather large window size degrades the spatial resolution of DOPU images.

Improvements of the spatial resolution of DOPU and segmented depolarizing tissue in B-scan images were achieved by introducing the concept of temporal DOPU.³¹ Temporal DOPU is realized by collecting multiple-frame data, e.g., 60 B-scan frames successively at the same position, so that a smaller evaluation window size in space (x, z) , even the minimum $1(x) \times 1(z)$ pixel, can still provide a sufficient number of Stokes vectors to be averaged.

A possible ambiguity in the realization of temporal DOPU has been discussed in Ref. 31: the true three-dimensional (3-D) size of the window used for calculating DOPU in the case of *in vivo* retinal imaging is not exactly known. Although the frames were registered in postprocessing to ensure pixel-to-pixel correspondence in (x, z) , the real location of the pixel in the y direction, perpendicular to the B-scan frame, was unknown due to the eye motion, and the use of a retinal tracker³²⁻³⁸ was suggested. An important factor to understand and analyze the results in terms of speckles called for more accurate estimation of the 3-D window size in comparison to the size of speckles and the numbers of independent speckles included in the averaging window volume. In the case of OCT intensity images, speckle noise reduction by multiple-frame averaging has been studied in relation to the locations of successive B-scans along the axis perpendicular to the B-scans,^{39,40} but no retinal tracker was employed.

It is the purpose of this study to analyze optimum conditions and parameters for DOPU imaging and segmentation of depolarizing tissue in the human retina. By use of a PS-OCT system with an integrated retinal tracker,³⁸ B-scan locations are stabilized to minimize the ambiguity of eye motion effects. This enables identification of optimum imaging and processing

*Address all correspondence to: Mitsuro Sugita, E-mail: n1142530@students.meduniwien.ac.at

conditions, as well as their relation to speckles. Sensitivity, efficiency, and susceptibility of DOPU imaging and depolarizing material segmentation are analyzed for a model eye and in the case of a healthy human retina. Furthermore, contrast-to-noise ratio (CNR) in the intensity images is also evaluated and analyzed. Based on the optimized parameters, we reveal new fine mapping of the RPE and Bruch's membrane (BM) in the living human retina.

2 Methods

2.1 Experimental Setup, Data Acquisition, and Postprocessing

The details of the setup of spectral domain PS-OCT (SD-PS-OCT) with an integrated retinal tracker have been published previously.³⁸ In this section, with a brief summary of the setup, we describe the data-acquisition protocols and conditions as well as the subsequent postprocessing used and performed for this study.

The setup consists of two main parts, an SD-PS-OCT with two detection channels for orthogonal polarization states (70 kA-scan/s), and a line-scanning laser ophthalmoscope (LSLO) for detection of the retinal position (70 frames/s) and corresponding eye tracking. In-plane retinal position displacement is obtained from the LSLO images [field of view (FOV): $8 \times 6 \text{ mm}^2$; $800 \times 600 \text{ pixel}^2$], and correction signals for cancelling the motion artifacts are sent to the OCT imaging scanner (not synchronized with the OCT acquisition) so that the same B-scan position on the retina can be kept during the acquisition.

Although the correction is conducted for displacements in both of the xy -directions, residual motion artifacts remain due to (1) motions in the depth (z) direction, (2) torsional eye motions (rotation in xy -plane), and (3) imperfect corrections for the xy -displacement. Postprocessing registration among B-scan images performed in this study can remove reasonable parts of (1) and the x -displacement of (3).

A B-scan is obtained by recording 1024 A-scans along the x direction (FOV: 8 mm, pixel size: $7.8 \mu\text{m}$; 56 B-scan frames/s, data acquisition performed during only one way of the asymmetric round trip scanner motions, not synchronized with the LSLO). Figure 1 shows the schematic view of the scanning

protocols with and without intentional shifting in the y direction. Multiple B-scan frames were repeatedly acquired near the foveal center. When no intentional shifting was applied [Fig. 1(a)], recording of B-scans were simply repeated at the same location as in a single line. In the case of a small intentional shifting in the y direction [in-plane direction orthogonal to the scanning direction (x)], the locations of the recorded B-scans were distributed over parallel lines [Fig. 1(b)]. The amount of shifting, dY , was set to 0, 17, or $34 \mu\text{m}$ [corresponding to the range covered by one series of B-scans ($N = 83$ or 50, for human retina or model eye, respectively)]. The lateral optical resolution of the system (theoretical size of the focused optical beam spot on the retina; $1/e^2$ -intensity full-width) was $17 \mu\text{m}$. So, in other words, the used parameters of the shift dY were 0, 1, and 2 optical spot sizes. The wavelength of the OCT was $860 \pm 30 \text{ nm}$ (FWHM), which corresponds to a depth resolution of $4.0 \mu\text{m}$ assuming a Gaussian spectrum (in tissue; refractive index $n = 1.38$). The pixel size in the depth (z) direction was $1.4 \mu\text{m}$ (in tissue).

Figure 2 illustrates the overall data processing steps. After the data acquisition of a series of B-scans, reconstruction of the SD-OCT intensity images was conducted; then a reference frame was selected manually by a visual check of the distortion and the depth in the B-scan; a frame exhibiting a retinal image with a small distortion and in an appropriate depth range is selected. In the next step, cross-correlation between each B-scan frame and the reference frame was evaluated. The peak value of each cross-correlation was used to select the best 50 frames out of 83; the frames with the 50 highest peak values of cross-correlation and other frames were excluded in further processing steps. Then, registration of each of the best 50 frames to the reference frame was performed based on the cross-correlation information.

For the single frame processing results in the study, reference frame data were used. In addition to the intensity image, a DOPU image was generated, using an 8×10 (x, z) pixel evaluation window ($\approx 63 \mu\text{m} \times 14 \mu\text{m}$) for a sliding average of the Stokes vectors over the B-scan. The details of the method and equations for the Stokes vector and the DOPU calculations are explained elsewhere.¹⁶ The conditions for intensity thresholding to avoid the inclusion of erroneous pixels in the DOPU evaluation window (i.e., Stokes vector averaging window) for

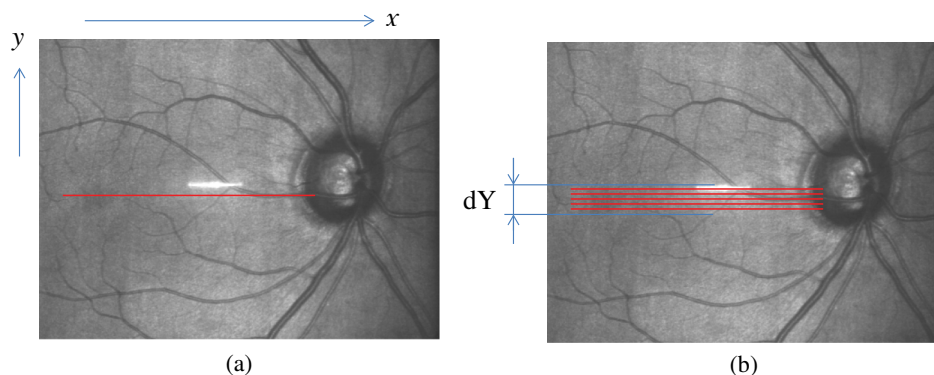


Fig. 1 Schematic of multiple B-scan acquisition protocols used in this study. Red lines indicate optical coherence tomography (OCT) B-scans. (a) B-M-mode scan: only x -scanner is actuated to scan the same location repeatedly. (b) B-M-mode scan with intentional shift dY : y -scanner is also actuated to apply small shift in y -direction. dY corresponds to the y -directional range of B-scans in a set of acquisition. dY in the figure is not to scale; it ranged from 0 to $34 \mu\text{m}$ for *in vivo* measurements. The *en face* fundus image is taken by line-scanning laser ophthalmoscope used for retinal tracking in this study.

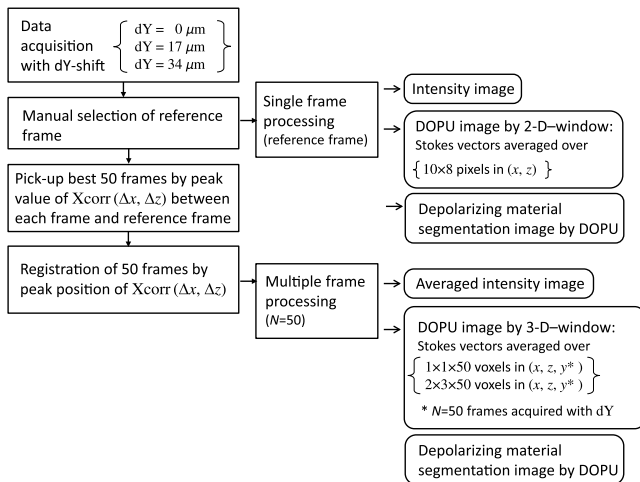


Fig. 2 Data processing steps and output images.

this study were (1) intensity value of 7 dB above the mean noise level is used for the threshold to exclude erroneous pixels and (2) the number of pixels having intensities above the threshold within a DOPU evaluation window should be $>12.5\%$; otherwise, the DOPU evaluation was regarded as void [the corresponding pixel (i.e., the center pixel of the DOPU evaluation window) is treated as background and shown in gray color in DOPU images]. For multiple-frame processing, the best 50 intensity images were averaged (in linear scale), and DOPU images were generated by using evaluation windows extending over either 1×1 or 2×3 pixels in the (x, z) directions and over the 50 frames (i.e., including temporal extent and spatial extent in y direction by the intentional shift dY). For example, in the 2×3 pixels case, the Stokes vector averaging includes $2 \times 3 \times 50 = 300$ vectors to assess the DOPU value.

After obtaining DOPU images, depolarizing material segmentation was done by thresholding. Areas of DOPU <0.75 were considered as depolarizing.^{16,27} For the resulting DOPU and segmented images, qualitative comparison and quantitative analysis based on the numbers of segmented pixels were conducted. The number of segmented pixels in a given image is a figure of merit in this study; when it is small, the sensitivity or detection capability of the depolarizing material is low, and vice versa.

A counter figure of merit against the sensitivity, chosen in this study, is spatial resolution. The DOPU window size (3-D volume) and its inverse are employed to represent this figure, because averaging within larger windows causes more blur in the image, implying a lower spatial resolution. For normalization, we introduce a unit for 3-D volume, optical resolution volume (ORV), which is defined by the product of optical resolution sizes of the OCT system in each x , y , and z direction, i.e., a spot size $17 \mu\text{m}$ (≈ 2.2 pixels) in x , $17 \mu\text{m}$ in y , and an optical depth resolution of $4 \mu\text{m}$ (≈ 2.9 pixels) in z , which totals $1156 \mu\text{m}^3$, corresponding to 1 ORV in this case. Since the typical speckle size in 3-D equals ~ 1 ORV,⁴¹ analysis using the unit of ORV is expected to make it easier to understand the results and the mechanisms in relation to speckles.

The number of segmented pixels (segmentation sensitivity) was plotted and analyzed against the DOPU window size in units of ORV (spatial resolution). The 3-D window volume is defined as the volume spanned by the centers of the involved voxels plus a positive offset of one optical resolution for

each dimension (i.e., $\approx \{[(l-1)/2.2 + 1] \times [(m-1)/2.9 + 1] \times (n+1)\}$ ORV for $l \times m \times n$ pixel window and shift dY of n times spot size). The centers of the voxels correspond to the centers of the light beams, and optical broadening of each beam, which corresponds to the offset, should be convolved; this broadening includes the possible light paths that contribute to the depolarization evaluated by DOPU. Under an exemplary condition: 1×1 (x, z) window and no shift dY , the effective volume of the window is not zero but is broadened and ranges over one optical resolution (equivalent to the offset). Consequently, the plots in Fig. 7 start at 1 ORV on the horizontal axis.

For the single-frame as well as the multiple-frame-averaged intensity images, CNRs (Refs. 40 and 42) were calculated in log10 scale for further analysis. Similar to the segmentation sensitivity analysis described above, CNR is plotted against the averaging window size; in order to keep the same windows and ORV size as in the DOPU analysis, 2×3 (x, z) window averaging was further applied to each of the single-frame and multiple-frame averaged images before calculating CNR.

2.2 In Vivo Retinal Imaging

Three eyes of healthy volunteers were imaged. The study was approved by the university's ethics committee and conformed to the Declaration of Helsinki for research in human subjects. The power to the eye is 0.4 mW from the LSLO and 0.7 mW from the PS-OCT. This is below the safety limit for combined exposures designated by the International Electrotechnical Commission.⁴³

The PS-OCT system used in this study is equipped with an internal fixation target display device utilizing an organic light-emitting diode micro display, and a static white, blinking cross pattern is projected on the retina during the acquisition (corresponding to the fixation target condition "FT1" in Ref. 38). The real spatial extent that the DOPU evaluation window involves for multiple frames is dependent not only on the (x, z) window size and intentional shift dY , but also on residual retinal motion after applying eye tracking for *in vivo* measurement. If the residual motion is large, then the effective window size is widened. In the current study under the static fixation target condition, the residual motion of the healthy eyes corresponded to ~ 0.7 to 1.5 pixels in the x direction and is estimated to be similar in the y direction.³⁸

Registration error for multiple frames causes another widening of the effective DOPU window. The cross-correlation was calculated by one pixel pitch in (x, z) ; therefore, the postprocessing registration resulted in residual errors of about one pixel size for the x and z directions when the residual motion after tracking is larger than 1 pixel.

2.3 Model Eye Imaging

A glass lens model eye, the imaged surface of which is covered with a thick monolithic semitransparent light scattering layer (~ 1 mm thick) consisting of epoxy based photo-curing resin and titanium dioxide particles (0.2 micron size, 0.15 wt%), mediated by a metallic thin film (chrome) at some locations to form an in-plane mask pattern (e.g., bars), was prepared. The optics is equipped with lenses to model the anterior segment and a sphere-shaped lens to model a vitreous body, and has a focal length of 23 mm.

The measurement protocol is exactly the same as that used for the *in vivo* retina, while the shift dY was adjusted so that 50

consecutive B-scans, instead of 83 in the case of the *in vivo* retina, cover the ranges of, e.g., 0, 17, or 34 μm in the y direction. This is because there is no practical eye motion and no need to exclude any acquired B-scan frames in this case; all 50 frames were used for the averaging and DOPU processing without discarding any frames (unlike the reduction from 83 to 50 in the case of the *in vivo* retina). Intentional shifting dY is set to be 0, 2, 4, 8, 17, 34, 51, and 68 μm , which corresponds to 0, 1/8, 1/4, 1/2, 1, 2, 3, and 4 optical spot sizes.

3 Results

3.1 In Vivo Healthy Retina

Figure 3 shows images obtained from healthy eye 1. The single-frame DOPU image [Fig. 3(g)] exhibits a well-distinguishable contrast between the region at the location of the RPE layer (low DOPU) and the regions of other layers (high DOPU). The DOPU images from multiple frames [Figs. 3(a)–3(f)] demonstrate higher spatial resolution owing to the narrower evaluation windows than that in the single-frame case.³¹ While the structures appear finer, Fig. 3(f) has features similar to Fig. 3(g); a thick band of green color (DOPU ~ 0.4 to 0.75) resides around the RPE cell layer, and blue-colored patches (e.g., DOPU ~ 0 to 0.4) appear at the center of the band. The similarity decreases when the shift dY becomes smaller [from Fig. 3(f) to Fig. 3(d), from Fig. 3(c) to Fig. 3(a)] and the (x, z) spatial window becomes smaller [from Fig. 3(f) to Fig. 3(c), etc.] The largest difference is observed between Figs. 3(f) and 3(a). The most noticeable difference is a decrease of the blue-colored patches and the appearance of yellow-red colored (e.g., DOPU ~ 0.75

to 1) patches instead. When the corresponding images of depolarizing material segmentation are checked, these changes are illustrated more clearly. While Fig. 3(m) keeps the thick segmented RPE band as seen in Fig. 3(n), it is shown in Fig. 3(h) that the depolarizing tissues are fragmented, especially around the center of the band. It is also observable in Fig. 3(h) that there are more fragmentations and less depolarizing material segmented at the edges of the thick band (i.e., around the interfaces from RPE cell layer to photoreceptor layer and to choroid) than in Fig. 3(m).

By further looking at transitions from Figs. 3(a) to 3(f), and from Figs. 3(h) to 3(m), the changes and differences between the neighboring conditions are relatively large up to Figs. 3(d) and 3(k), while rather small changes are observed between Figs. 3(e) and 3(f), and Figs. 3(l) and 3(m). In other words, the saturation point is around Figs. 3(e) and 3(l). It can be said that those images, beyond the saturation point, are less susceptible to the fluctuation of the imaging and processing conditions. The similarity to the single-frame processed image, Figs. 3(g) and 3(n), is also high for those images with low susceptibility.

Figure 4 shows the results of healthy eyes 2 and 3. It is observed that the overall features and characteristics are similar to those found in the results of healthy eye 1.

3.2 Model Eye

Imaging results in the model eye are shown in Figs. 5 and 6 for the DOPU and depolarizing material segmentation images, respectively. A transition with a large change of DOPU and segmented pixels is observed from $dY = 0$ to 3 spot sizes for the 1×1 window case [Figs. 5(a)–5(f) and Figs. 6(a)–6(f)], and

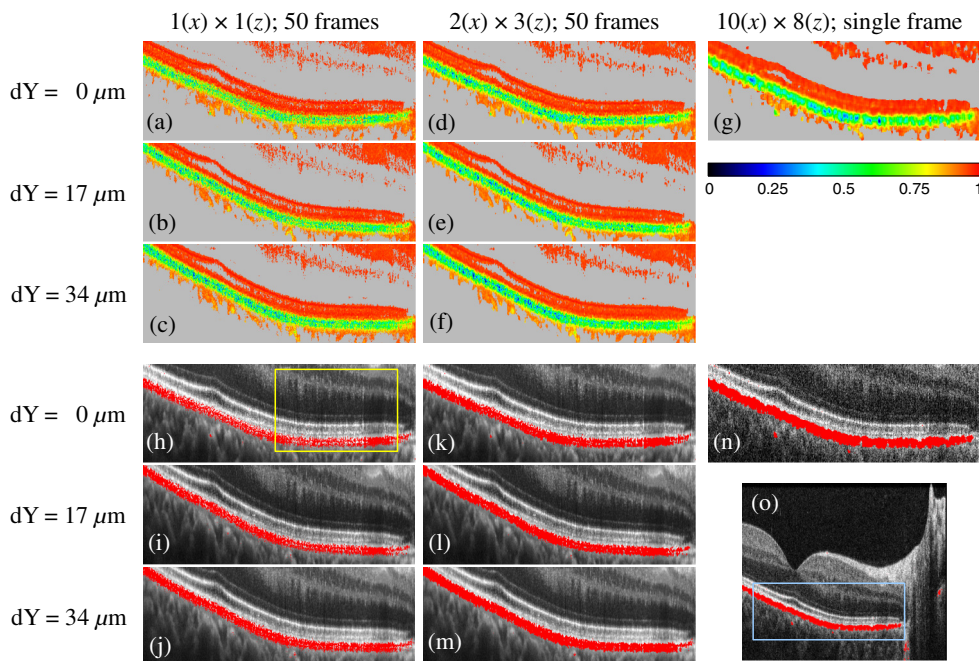


Fig. 3 Images in healthy eye 1. (a) to (g): Degree of polarization uniformity (DOPU). (h) to (o) Depolarizing material segmentation overlaid on intensity image. Red pixels show segmented depolarizing material. DOPU evaluation window in (x, z) : 1×1 pixel for (a) to (c) and (h) to (j), 2×3 pixels for (d) to (f) and (k) to (m) with 50 frames processed; 10×8 pixels for (g), (n), and (o) with single frame processed. Intentional shift dY : 0 μm for (a), (d), (g), (h), (k), and (n); 17 μm for (b), (e), (i), and (l); 34 μm for (c), (f), (j), and (m). Color scale for DOPU: 0 to 1. Gray pixels indicate background pixels excluded by intensity thresholding. Light blue rectangle in (o) indicates enlarged area of (a) to (n). Yellow rectangle in (h) indicates enlarged area of interest in Fig. 13.

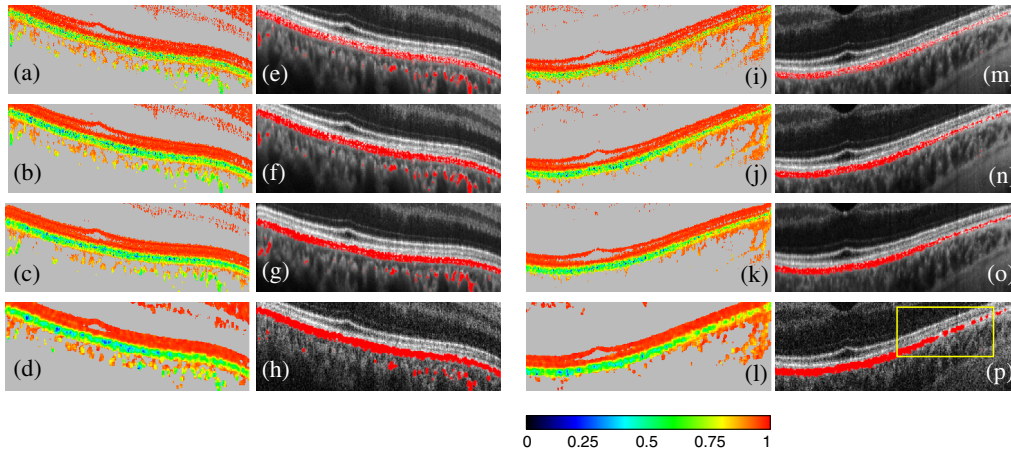


Fig. 4 Images in healthy eye 2 and healthy eye 3. (a) to (d) and (i) to (l) DOPU. (e) to (h) and (m) to (p) Depolarizing material segmentation overlaid on intensity image; red pixels show segmented depolarizing material. DOPU evaluation window in (x, z) : 1×1 pixel for (a), (e), (i), and (m), 2×3 pixels for (b), (c), (f), (g), (j), (k), (n), and (o) with 50 frames processed; 10×8 pixels for (d), (h), (l), and (p) with single frame processed. Intentional shift dY : $0 \mu\text{m}$ for (a), (b), (e), (f), (i), (j), (m), and (n); $17 \mu\text{m}$ for (c), (g), (k), and (o). Color scale for DOPU: 0 to 1. Yellow rectangle in (p) indicates enlarged area of interest in Fig. 15.

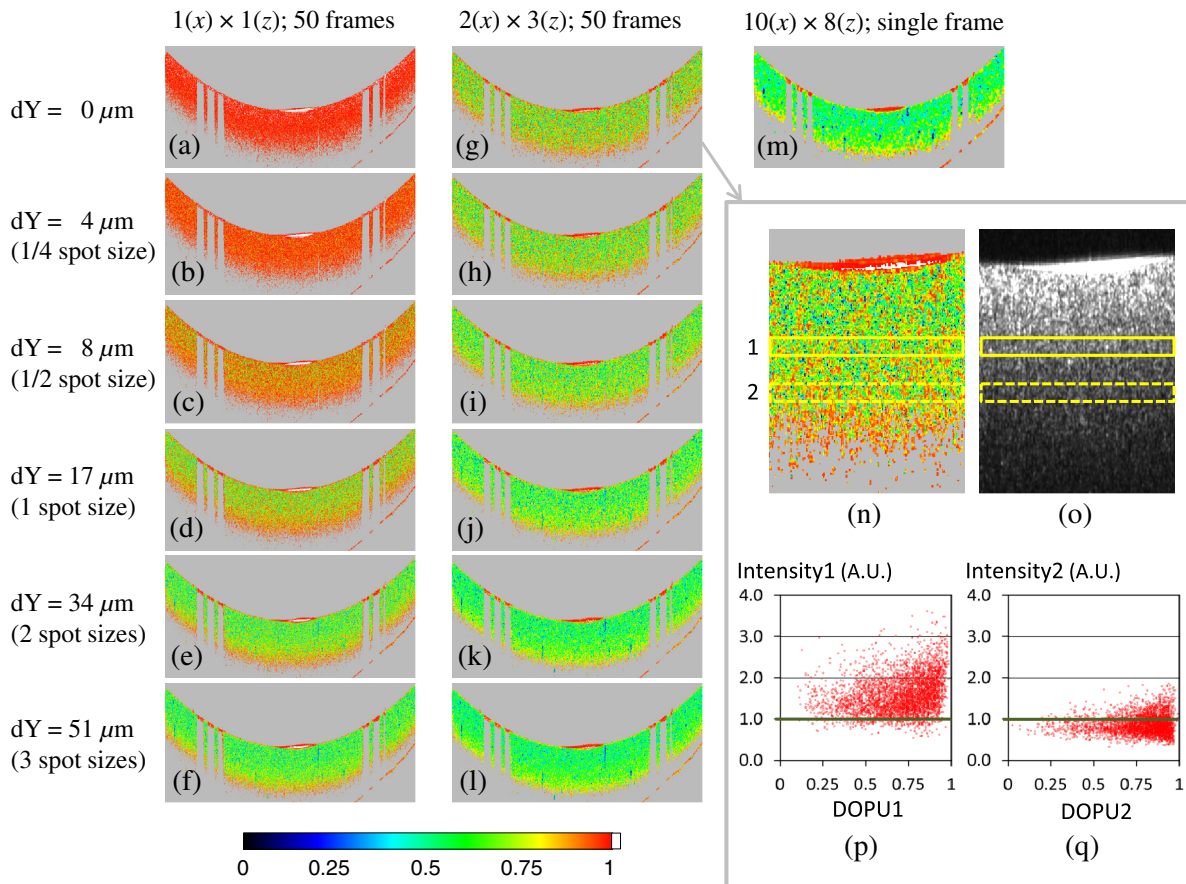


Fig. 5 DOPU images in model eye. DOPU evaluation window in (x, z) : 1×1 pixel for (a) to (f), 2×3 pixels for (g) to (l) with 50 frames processed; 10×8 pixels for (m) with single frame processed. Intentional shift dY : 0, 4, 8, 17, 34, and $51 \mu\text{m}$ for (a) and (g), (b) and (h), (c) and (i), (d) and (j), (e) and (k), (f) and (l), respectively. (n) to (q) Enlarged center part from (g) and corresponding quantities. (n) DOPU. (o) OCT intensity (linear scale). (p) and (q) DOPU-intensity maps of the pixels within the two regions indicated by solid (1) and dashed (2) yellow rectangles, respectively, drawn in (n) and (o). Intensity in (p) and (q) is on linear scale and normalized by the threshold value used for the DOPU evaluation (7 dB above the mean noise level). Color scale: 0 to 1.

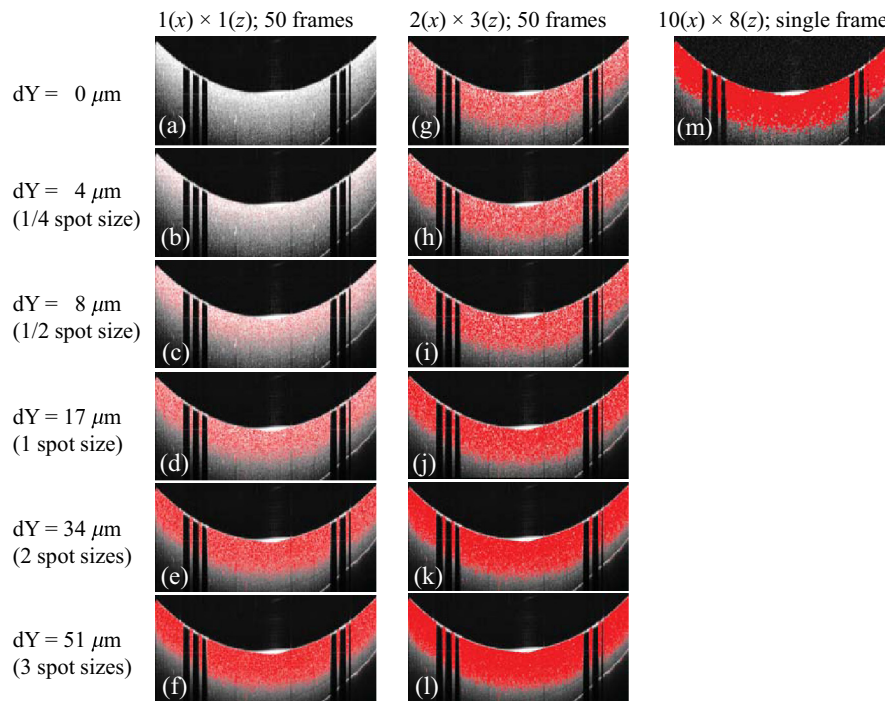


Fig. 6 Depolarizing material segmentation overlaid on intensity images in model eye. DOPU evaluation window in (x, z) : 1×1 pixel for (a) to (f), 2×3 pixels for (g) to (l) with 50 frames processed; 10×8 pixels for (m) with single frame processed. Intentional shift dY : 0, 4, 8, 17, 34, and 51 μm for (a) and (g), (b) and (h), (c) and (i), (d) and (j), (e) and (k), (f) and (l), respectively.

another noticeable change from 0 up to 1 spot size is found in the 2×3 window case [Figs. 5(g)–5(l) and Figs. 6(g)–6(l)]. The transition exhibits DOPU values changing from high to low and an increase of segmented pixels, when the 3-D window becomes larger. They nearly reached the values obtained in single-frame processed images with the 8×10 window [Figs. 5(m) and 6(m)].

This result can be explained by the origin of the DOPU parameter: it is the uniformity among the measured pixels (voxels) and is naturally high (i.e., they are uniform) if the measurement is a simple repetition of the exact similar location and condition. This is the case if the 3-D window is very narrow [e.g., a small dY and 1×1 (x, z) window].

On the other hand, it can also be seen that even in the narrowest window case, the DOPU values in Fig. 5(a) are not always exactly equal to 1 (pixels colored in white). This non-uniformity is mainly caused by fluctuations caused by non-deterministic noise, such as thermal noise and shot noise.

The increase of DOPU values observed near the deepest position [clearly visible in Figs. 5(d)–5(i)] can be explained by considering the single and multiple light scattering contributions: pixels dominated by single and multiple scatterings have high and low DOPUs, respectively.⁴⁴ It is reasonable, in this model eye, which has rather uniform scatterer distributions, that pixels dominated by multiple scattering have weaker signals than the pixels dominated by single scattering due to the attenuation in the scattering processes, when a comparison is made in the same depth of the image. Consequently, near the edge region on the deep side, the intensity thresholding used for DOPU evaluation¹⁶ suppresses the pixels with low DOPU (and, hence, low intensity) more strongly [see Figs. 5(n)–5(q)], leading to an apparently higher DOPU.

When a similar viewpoint on the saturation as explained for the *in vivo* healthy eye results is taken for observations of Figs. 5 and 6, this saturation point is at around Figs. 5(j) and 6(j). The high similarity to the single-frame result for low susceptible regions [i.e., Figs. 5(j)–5(l) and Figs. 6(j)–6(l)] can also be observed.

3.3 Quantitative Analyses

Figure 7 shows the results for the DOPU segmentation analysis. The number of segmented depolarizing material pixels is plotted as a function of volume of the DOPU evaluation window in Fig. 7(a). The data points acquired and processed by the same window size and intentional shift conditions are located differently in the horizontal axis. This reflects the variations of residual motions and registration errors among the model eye and the three *in vivo* eyes. The vertical axis is normalized by the number from the single-frame result [by 8×10 (x, z) window], so that the similarities of the multiple-frame averaged results to the single frame can be observed, which increases from 0 to 1 when the window volume increases. The overall distribution of the data points, including both the model eye and *in vivo* eyes, is relatively well congregated (fitted by a seventh-order polynomial with $R^2 = 0.975$, for the whole window volume range from 1 to 17.5 ORV) and appears as on a saturation curve.

In Fig. 7(b), two kinds of characteristics are plotted: (1) efficiency, defined by the segmentation sensitivity (i.e., normalized number of segmented pixels) divided by the window volume (i.e., spatial resolution loss as the cost), and (2) susceptibility, defined by the gradient of the fitted sensitivity curve in Fig. 7. The efficiency is expected to suggest an optimum condition that balances the segmentation sensitivity and spatial

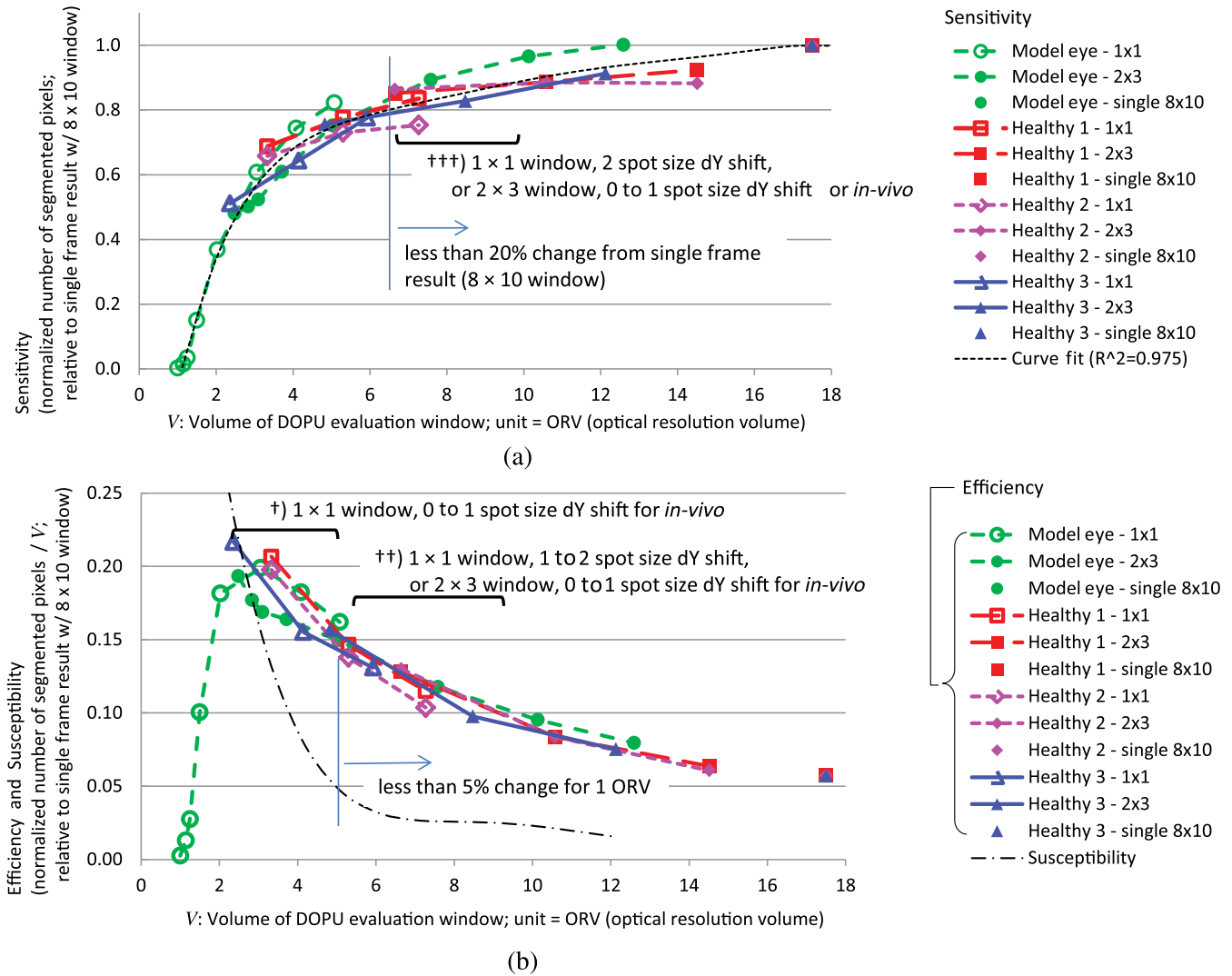


Fig. 7 Sensitivity, efficiency, and susceptibility of depolarizing material segmentation by DOPU. (a) Sensitivity. (b) Efficiency defined as sensitivity/ V , and susceptibility defined as gradient of sensitivity. Volume of DOPU evaluation window V includes an offset of 1 optical resolution volume optical spot broadening, and residual motions for *in vivo* eyes. All points of the single frame (8×10 window) coincide at the same position (no broadening by residual motion exists for single frame cases).

resolution, and it has a peak around the window volume of 2 to 4 ORV. The susceptibility indicates how much fluctuation is caused by the window volume change, for example, if the window volume fluctuates by 1 ORV at around 5 ORV (e.g., changing from 4.5 to 5.5 ORV), it will affect the segmentation result by $\sim 5\%$ of the number of segmented pixels.

Figure 8 shows the result for intensity images evaluated by CNR. The images and regions of interest (ROIs) used in the assessment of CNR are shown in Figs. 9 and 10. The ROIs are located so that they do not contain obvious features; if the speckles are neglected, they are intended to exhibit rather monotonic gray values. For the *in vivo* retina, the ROIs are from NFL and the inner plexiform layer. Although they are not adjacent to each other to express direct contrast, the ROIs in them are appropriate for CNR evaluation because of their OCT intensity and reasonable homogeneity. In the model eye, since there is no distinct structure of layers, ROIs are selected in different depths. The average intensities for the ROIs differ because of two factors: attenuation by light

scattering and reflection by the preceding segment, and sensitivity drop-off by limited resolution of the spectrometers for SD-OCT (Refs. 45 and 46) (the zero-delay position is at the top of the B-scan images).

The plot in Fig. 8 shows that CNR rises when the averaging window volume increases. On the other hand, the rise is not as steep as in the case of DOPU segmentation analysis in Fig. 7 and shows no distinct saturation. Curve fitting for each eye and all eyes was performed by the equation $CNR_{\text{normalized}} = V^p$, where V is the averaging window volume and p is the fitting parameter, and the result is summarized in Table 1. The power p ranges from 0.47 to 0.63, and the average is 0.54.

With regard to the quality of the image, in our opinion by visual check, the most preferable among Figs. 9(a)–9(i) is Fig. 9(e), and the optimum condition for a general purpose would be realized using 50 frame averaging with a 1×1 (x, z) window and a shift dY of 1 spot size. It should be noted, however, that the optimum depends, e.g., on the fixation capability of the subject.

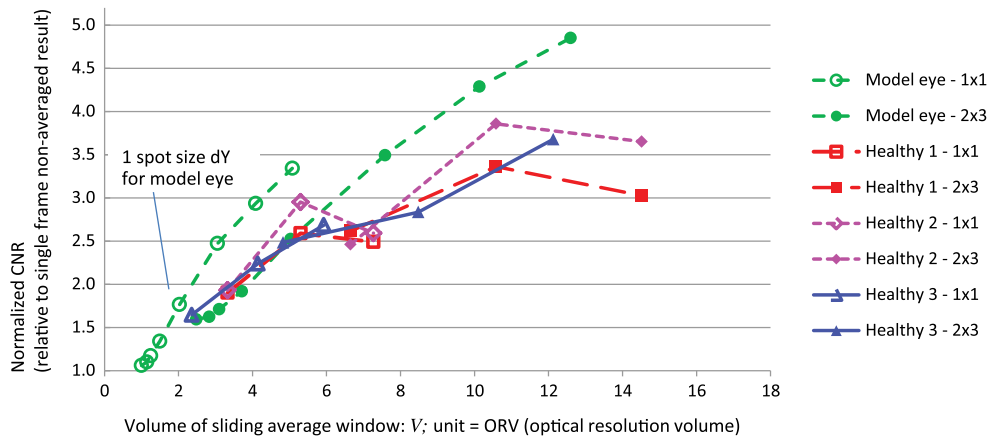


Fig. 8 Improvement of contrast-to-noise ratio (CNR) of intensity images by sliding window average as a function of window size. Regions of interest (ROIs) for intensity images are shown in Fig. 9 (*in vivo* eyes) and Fig. 10 (model eye).

4 Discussion

We have obtained DOPU and depolarizing material segmentation images using various 3-D evaluation windows and well-defined intentional shifting of the B-scan position in the y direction while the overall scan position was stabilized by a retinal tracker.

An interesting question which should be addressed first is whether the averaged pixels in the 3-D evaluation window over multiple frames, acquired sequentially in time, contribute to the results by real temporal changes of the samples, or by their spatial distribution (i.e., changes in y direction governed by the intentional shift dY and the residual motion caused by imperfect tracking). A clue is in the results presented in Fig. 7(a), where the results of the model eye and human eyes appear to share the same curve in a good approximation. Since the model eye used in this study is solid, there is basically no temporal change due to, e.g., liquid and particle motions. If the human retina has significant temporal change of its constituents (e.g., motions of

pigments in RPE cells in time) affecting the depolarization imaging, it should lead to deviation from the model eye result, which is not seen in Fig. 7(a). It is, therefore, expected that no major effect by the real temporal change of the samples were included in this study. An example of a contribution of a real temporal change in a local region of the image can be found in Fig. 11. In the DOPU and the corresponding segmentation images, it is observed that blood flow in the inner retinal layers cause an increase of depolarization and the segmented pixels around the RPE cell layer (indicated by yellow arrows), generating a visible difference compared to the adjacent RPE layer, although no difference within that layer is expected. The possible cause of this change would be modulation of the optical paths by the temporal change of the blood flow.

There are two points of further interest that this study and the results can shed light on. The first point relates to the question: “What is the optimum condition for imaging depolarizing materials and tissues and the subsequent data processing?” To answer

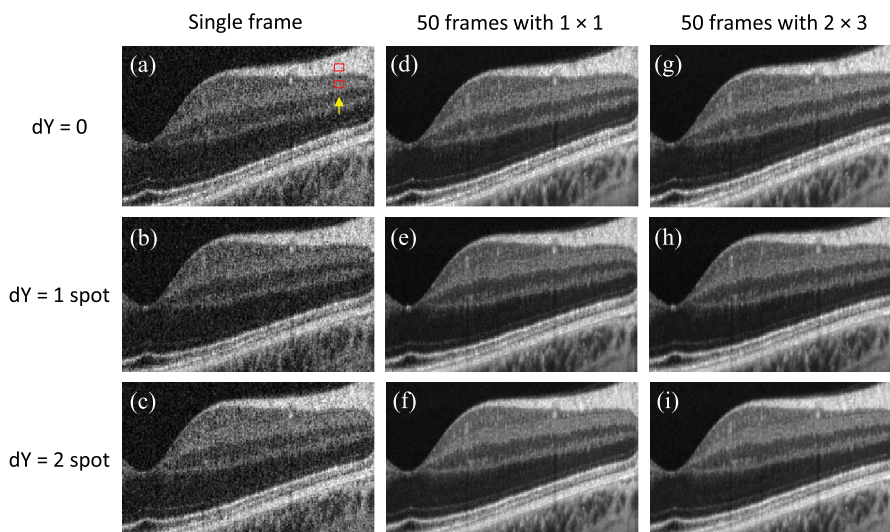


Fig. 9 CNR in intensity images in healthy eye 3. (a) to (c) Single frame images. (d) to (f) Images averaged over 50 frames. (g) to (i) Images averaged over 50 frames and averaged by 2×3 (x, z) pixel window. (a), (d), and (g) are acquired with no dY shift. (b), (e), and (h) are acquired with 1 spot size dY shift. (c), (f), and (i) are acquired with 2 spot size dY shift. Red rectangles in (a) marked by arrow indicate ROIs for CNR calculation; 20×15 (x, z) pixels each located in nerve fiber layer and inner plexiform layer.

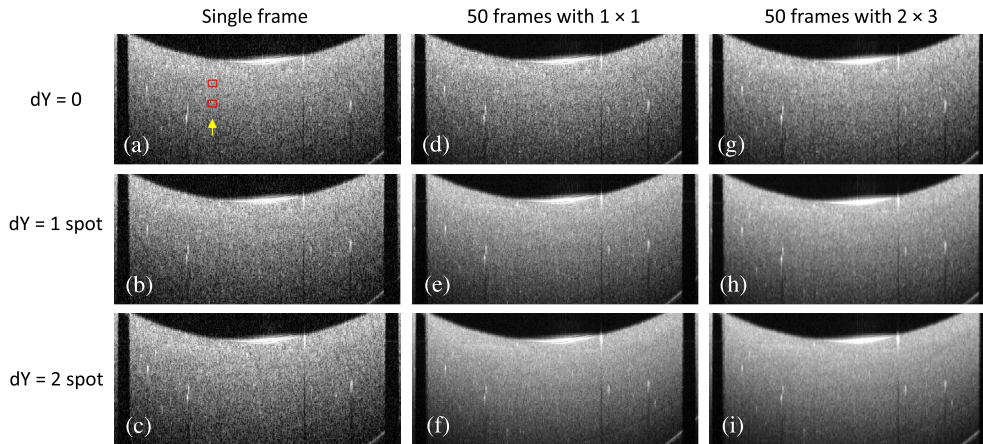


Fig. 10 CNR in intensity images in model eye. (a) to (c) Single frame images. (d) to (f) Images averaged over 50 frames. (g) to (i) Images averaged over 50 frames and averaged by 2×3 (x, z) pixel window. (a), (d), and (g) are acquired with no dY shift. (b), (e), and (h) are acquired with 1 spot size dY shift. (c), (f), and (i) are acquired with 2 spot size dY shift. Red rectangles in (a) marked by arrow indicate ROIs for CNR calculation; 20×15 (x, z) pixels each located in different depths.

this question, we checked the DOPU images and segmentation results from multiple-frame processing regarding their sensitivity, spatial resolution, susceptibility to fluctuation of the data-acquisition and postprocessing conditions, as well as by their similarity to the results from single-frame processing.

A figure of merit analyzed in Sec. 3 was efficiency, leading to the window volume of 2 to 4 ORV as an optimum. This condition corresponds to using the smallest window for *in vivo* eyes, i.e., a 1×1 (x, z) window and shift dY of 0 to 1 spot size [marked as † in Fig. 7(b)]. In this case, the physical extension of the evaluation window is caused solely by residual motion artifacts and cross-correlation errors of the averaged frames. On the other hand, this condition would not be the best if susceptibility is included into consideration.

Susceptibility is a measure of how repeatable segmentation results are and is especially important if the imaging of real patients is considered. The fixation capability and performance of retinal tracking differ widely among patients, causing variations of residual motions. In the case of large residual motions, the effective DOPU evaluation window is widened. If the susceptibility is high, this widening results in significant variations between repeated DOPU images and subsequent segmentation of depolarizing tissues, making segmentation less reliable. An estimation of the optimum window volume parameter, considering the effect of this widening, is given in the following.

Table 1 Curve fitting results with $\text{CNR}_{\text{normalized}} = V^p$.

	p	(R^2)
Model eye	0.63	(0.95)
Healthy eye 1	0.47	(0.79)
Healthy eye 2	0.52	(0.83)
Healthy eye 3	0.53	(0.94)
Average	0.54	
All eyes	0.54	(0.77)

While the widening in the x and z directions is suppressed and limited by postprocessing registration, which leaves only one pixel error, the residual motion in the y direction cannot be corrected by postprocessing. When the residual y -motion is increased from a 0 to 1 spot size,³⁸ the window volume changes by 2 ORV for the 1×1 (x, z) window or by 4 ORV for the 2×3 (x, z) window (see Fig. 7, the separations between the neighboring data points for different shifts dY in the human eyes). Since the susceptibility is defined as the sensitivity change per unit window volume change (in ORV), 5% susceptibility corresponds to 20% change (of sensitivity) in the case of 4 ORV window volume change. The susceptibility curve in Fig. 7(b) shows that if 5% susceptibility is set as a maximum tolerance, for example, a window volume parameter > 5 ORV is required in the DOPU calculation [e.g., conditions marked as †† in Fig. 7(b)]. This estimation, therefore, indicates

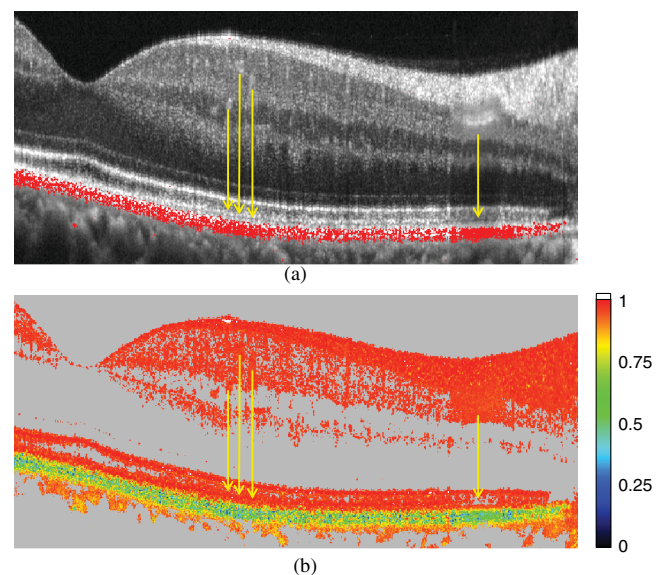


Fig. 11 Possible contributions from the inner retinal layers to DOPU in the outer layer. Yellow arrows: low DOPU regions with blood flow fluctuations in the inner layer. Images in healthy eye 1 [Figs. 3(h) and 3(a)]. (a) RPE segmentation. (b) DOPU.

a larger window volume parameter than that obtained as an optimum for the maximum efficiency (i.e., 2 to 4 ORV).

Another example of high susceptibility in the case of employing the smallest window size is the appearance of more segmented pixels in Fig. 11. The difference between the adjacent regions in the RPE layer, i.e., the region affected by blood flow and the region not affected, can be noticed in Fig. 11, which is an enlargement of Fig. 3(h), while it is less observable in Figs. 3(l)–3(n), which are processed with larger evaluation windows.

The above-mentioned changes and variations in the RPE layer caused by residual motions or by inner retinal layer contributions disturb stable evaluation and segmentation of the images, both qualitatively and quantitatively, for small evaluation window sizes.

Another factor impacting the selection of the window volume parameter (imaging and processing conditions) might be the similarity to the single-frame processed image when the backward compatibility to previous clinical studies carried out by single-frame data analysis (e.g., Refs. 18, 25, and 27–30) is required. For example, if a difference $\leq 20\%$ between the sensitivities or the numbers of segmented pixels by single-frame and multiple-frame evaluations is requested, the window size must be >6 ORV [e.g., conditions marked as ††† in Fig. 7(a)]. This is larger than those obtained for the maximum efficiency (window size: 2 to 4 ORV) and for $\leq 5\%$ susceptibility (window size: <5 ORV). These analyses of three conditions for the optimum window volume parameter in the DOPU calculation indicate trade-offs, and thus, one should choose the parameter depending on which figure of merit is required to be optimized.

When we try to include the result of the CNR analysis further in the above criteria, a larger window volume seems advantageous. However, although CNR is improved by the larger window volume, the resolution is degraded, leading to a similar trade-off as in the case of DOPU imaging and depolarizing tissue segmentation.

Another point we should be aware of when realizing an optimum condition is that data-acquisition conditions (i.e., dY shift) must be defined before the measurement of a patient eye, while postprocessing parameters [i.e., (x, z) window size, or registration accuracy] can be changed afterward to optimize each figure of merit of interest.

As a conclusion, an optimum window volume for a general purpose would be ~ 6 ORV ($\sim 1.8^3$ ORV), which can be realized by using nominal (i.e., not including optical broadening) window size parameters having an extent of about a half optical resolution for each dimension (e.g., in this study by our system, conditions close to the criteria are x : 2 pixels, z : 3 pixels, dY: 0 spot size and x : 1 pixel, z : 1 pixel, dY: 1 spot size) assuming an additional broadening by residual motion or registration error ranging from 0.3 to 0.5 times the optical resolution for each dimension.

The result of the saturation curve in Fig. 7 deserves further discussion especially with regard to speckles. According to a previous study using phantoms containing melanin granules or latex particles, the mechanism causing depolarization was suggested to be multiple scattering by those embedded particles.⁴⁴ The hypothesis is that in the multiple-scattering process, the polarization is very sensitively modulated by even small changes of the optical path or beam incident condition. This can be explained by considering that a single-scattering process by a dielectric structure having a size of the order of the

wavelength as the elementary process of the multiple scattering has a relatively strong polarization dependence on scattering angles (e.g., by the theories and approximations of Mie and Rayleigh scattering regimes),^{47–49} and each scattering angle at the constituent single-scattering process ranges widely in a turbid medium, where the scattering paths are randomly distributed. Thus, the resulting polarization states range broadly, depending sensitively on the positions of incidence (i.e., pixel location). In such situations, where multiple scattering dominates, speckles will naturally be strong and fully developed in the obtained image, since they also originate from amplitude and phase modulations by multiple scattering.

An important point is that the speckles are not just random noise, in this context; they carry information on the sample optical properties. The averaging of the Stokes vector (and using the norm of the averaged vector), in evaluation of DOPU, is a mathematical operation that can represent the randomness or uniformity of the vectors; e.g., in case of a vector norm ≈ 1 for the averaged vector, the vectors have similar orientation and the backscattered light is in a well-defined polarization state, whereas in the case of a short vector norm (i.e., far from 1) for the averaged vector, the vectors are randomly oriented and the backscattered light is depolarized. Therefore, the meaning of this averaging operation is rather different from, e.g., the averaging of OCT intensity for speckle noise reduction. Thus, the speckle patterns, imaged in the two orthogonal polarization detection channels, contain the information on the property of optical samples, and the information is decoded by, e.g., taking the ratio of the two interference signal amplitudes for retardation.

In the following, we provide a simplified analysis of the DOPU behavior as a function of window size in terms of a simplified speckle model (Fig. 12), where DOPU is replaced by uniformity or randomness of polarization states along the one-dimensional spatial extent, and the polarization state is represented only by retardation. Speckle patterns are generated by two orthogonal polarization states and detected by PS-OCT; the resulting retardation distribution derived by PS-OCT is analyzed. In this model, the speckle pattern is expressed as either (1) a sinusoid as a function of position in the xy -plane, and the highest spatial frequency (determined by the optical spot size or lateral optical resolution) of the speckles is employed [Fig. 12(a)], or (2) evenly adding two sinusoids: one with the highest frequency and the other with $1/2.3$ of the highest frequency [the ratio 2.3 is chosen for a generalization: in order to avoid exact harmonics (e.g., 2 or 3), which would lead to a special condition]. The difference of the speckle patterns generated by the two polarization states is modeled as a relative shift in space, e.g., 0.3 spot sizes in this example (similar to above, chosen from aliquant numbers). Retardation is calculated by the arctangent of the ratio of signal amplitudes of the two polarization states.^{1,5} In case (1), retardation changes by the full range from 0 to 90 deg with a period of 1 spot size. Here, in this simplified model, the behavior of polarization uniformity is determined solely by this retardation change in space, so we expect that the uniformity decreases according to the widening of the averaging width from a 0 to 1 spot size, because the retardation changes over the whole range (0 to 90 deg) within that width. When the averaging is performed over a larger volume beyond the 1 spot size, the polarization uniformity is not decreasing any further, since the retardation variations within the larger volume will be similar. The distribution of retardation values included in

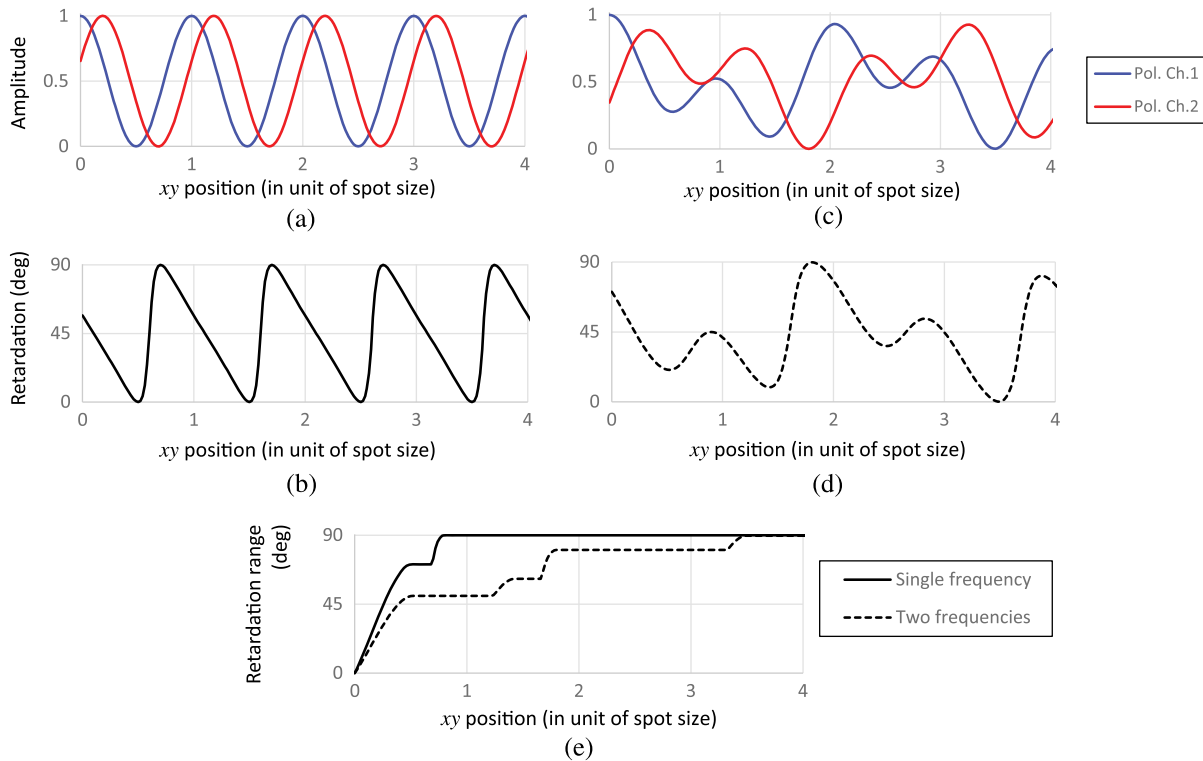


Fig. 12 Simple modeling of speckles and polarization change as functions of position in xy -plane. (a) and (c) OCT signal amplitudes for two polarization channels 1 and 2. (b) and (d) Retardation. (e) Ranges of retardation. Speckle pattern is modeled by single sinusoid of the highest spatial frequency for (a) and (b), and evenly added two sinusoids of the highest and $1/2.3\times$ the highest frequency for (c) and (d). Each sinusoid of channel 2 is shifted by 0.3 spot size in xy -position against the corresponding sinusoid of channel 1 for both the highest and $1/2.3\times$ the highest frequencies.

the averaging volume is expressed in Fig. 12(e) in terms of the accumulated range of retardation, and it shows a saturation behavior as discussed above.

It is assumed, in case (1), that speckles are fully developed by abundant multiple-scattering processes, which dominate other single-scattering processes, so that the amplitudes undergo full modulation (i.e., contrast of the sinusoid is 100%, and the amplitudes range from 0 to 1 without an offset). In case that the modulation is not full, where lower spatial frequency components play a role, e.g., in case (2), which employs a 50:50 mixture of the two sinusoids, the saturation observed in Fig. 12(e) is slower as compared to that in case (1), because the amplitudes only reach the full range 0 to 1 at ~ 3.5 spot sizes as does the retardation.

This brief analysis is in agreement with the overall behavior of the DOPU segmentation sensitivity in Fig. 7(a), which has a steep rise from 1 to 3 ORV window volumes corresponding to dY shifts from 0 to 2 or 3 spot sizes, and the following saturation; even this simple model can explain the essential features and the mechanism and suggests that the dominating spatial frequency of the speckle patterns is equivalent to 1 to 3 spot sizes.

In contrast to the saturation behavior of the DOPU segmentation sensitivity, the behavior of CNR in Fig. 8 does not exhibit obvious saturation. The CNR of intensity images improves with averaging window volume according to a power law with a power of ~ 0.54 . This result agrees well with previous analyses, stating that the noise reduces according to the square root of the number of independent speckles to be averaged.^{41,50,51} The

averaging window volume units of ORV, used in this study as the parameter in Fig. 8, corresponds to the number of independent speckles when the speckles are well developed and have a typical size of 1 ORV three dimensionally, making the agreement consistent.

The differences of the fitted power p among the eyes, ranging from 0.47 to 0.63 in Table 1, can be explained as follows: in reality, the ROIs contain real features (i.e., structures like capillaries, etc., which are not regarded as speckles) larger than the speckle size and smaller than the size of the ROI, the distribution of which are different among model eye and human eyes, leading to different end points, i.e., the CNR curves are not necessarily exactly equal.

Another factor for the model eye used in this study is that the difference of OCT intensities in the ROIs originates from a rather continuous drop-off of the SD-OCT sensitivity change in depth and attenuation by the preceding scatterers. Such a continuous drop-off also causes a gradient within each of the ROIs along the depth. The gradient adds an offset to the intensity variances in the ROIs, and so lowers the CNR. The usage of a model eye with a more elaborate multilayer coating for the modeled retina⁵² would enable a condition closer to that of the *in vivo* retina.

The second point of interest this study should shed light on is to investigate and to interpret the higher-resolution images obtained by the different 3-D evaluation windows for DOPU, especially in the case of the smallest 3-D window [i.e., 1×1 (x, z) window and ($dY = 0$)]. Since the images obtained under that condition show somewhat different DOPU distribution and

segmentation results for depolarizing material than those formerly seen in the images processed by single-frame evaluation windows, it can lead to new understanding of the tissue structures and characteristics, as well as the mechanism of how the depolarization evolves in the retinal layers.

The most noticeable difference observed is the decrease of depolarizing tissue in the thick band region around the RPE cell layer, especially the appearance of many breaks and fragmentations in the middle of the band. The question of whether this broken structure means a real RPE loss or not is critical when the segmented images are to be used in clinical situations. A possible interpretation is explained using Fig. 13, where enlarged images of intensity and depolarizing material segmentation [Figs. 13(d) and 13(f)] are displayed along with corresponding intensity and DOPU profiles as functions of depth [Fig. 13(e); generated by averaging over 100 horizontal pixels].

The photoreceptor inner and outer segment junction (IS/OS), the cone photoreceptor outer segment tips [COST; or Verhoeff's membrane (VM)], and the rod photoreceptor outer segment tips (ROST),^{53,54} indicated in Fig. 13, are interfaces between the retinal structures. They exhibit hyper-reflective peaks in the intensity profile and show local increases and peaks at the corresponding positions in the DOPU profile. These correlations between the intensity and DOPU profiles are in agreement with previous reports, which have shown that these structures exhibit polarization-preserving reflections;^{16,44} these reflections occur at interfaces that do not consist of thick cells and a rather simple single-scattering process is expected.

BM, consisting mainly of elastic fibers, is a thin (2 to 4 μm) acellular matrix⁵⁵ and, therefore, is expected to also exhibit polarization-preserving reflection. In Fig. 13, it can be observed that the BM has a hyper-reflective peak in the intensity profile and exhibits a local increase with a peak at the corresponding position in the DOPU profile, suggesting a polarization-preserving reflection. Contrary to other polarization-preserving reflections, the DOPU peak of the BM is within a wide valley [e.g., shown as the blue dashed curve indicated by ‡ in Fig. 13(e)].

This wide valley corresponds to the depolarization caused by the RPE cells (e.g., shown in Ref. 44 with a comparison between normal and albino human retinas, where an albino retina does not have a typical low DOPU distribution around the RPE); the RPE cell layer also exhibits a hyper-reflecting peak in the intensity profile, while a local decrease and a valley are around the corresponding position in the DOPU profile. Two noticeable features of this DOPU valley profile are (1) the width of the valley is larger than those of the intensity peaks of other layers and (2) the depth position of the local minimum is displaced from the peak position of the intensity profile.

These features suggest that the contribution from the RPE cell layer to the intensity profile should spread wider than other hyper-reflective peaks and should have a tail toward the deep side of the maximum position, e.g., the blue dashed curve indicated by † shown in Fig. 13(e). This wide profile with tailing and the shifted peak positions between the intensity and DOPU profiles can be explained by taking the multiple-scattering processes by the pigments (melanin granules) contained

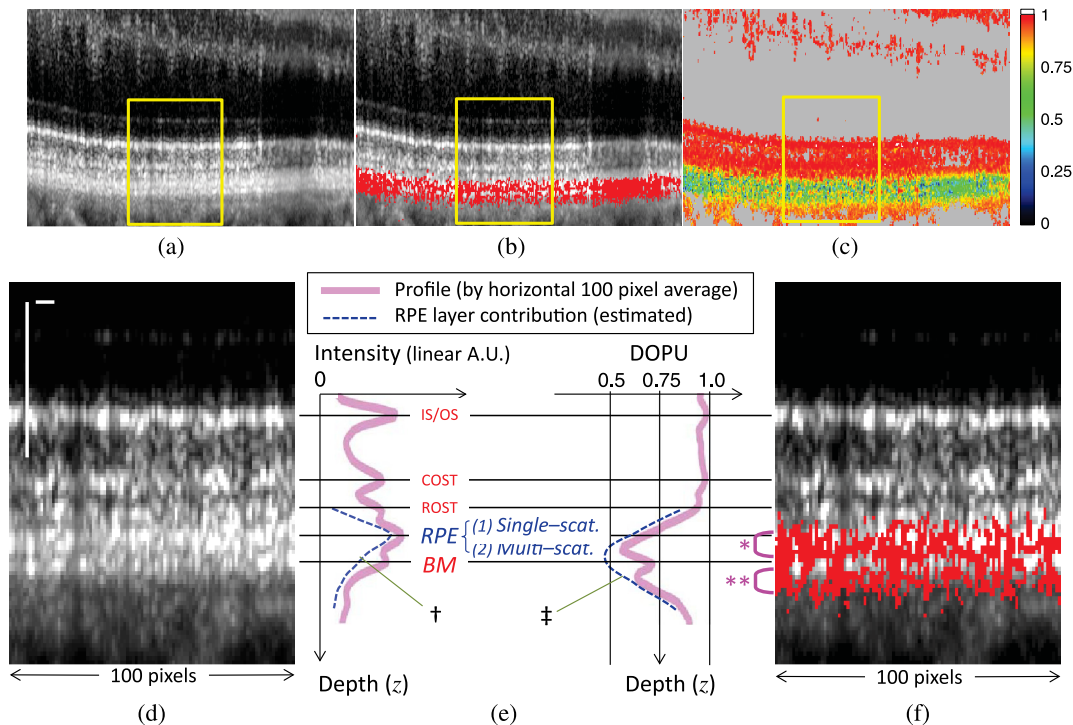


Fig. 13 Comparison of enlarged images in healthy eye 1 for the detailed locations of retinal layers and their depolarization properties. (a) and (d) Intensity: 50 frame processed images with 1×1 (x, z) window, acquired with $dY = 0$. (b) and (f) Depolarizing material segmentation. (c) DOPU. Yellow rectangle indicates area shown in enlarged images (d) and (f). Charts in (e) illustrate estimated contributions from involved retinal layers in comparison to the depth positions in (d) and (f). Magenta brackets indicate depth ranges of the double-layer: *Inner layer above Bruch's membrane, and ** outer layer below Bruch's membrane. Scale bars: 50 μm . Color scale (DOPU): 0 to 1. RPE, retinal pigment epithelium; BM, Bruch's membrane; IS/OS, inner/outer segment junction of photoreceptors; COST, cone photoreceptor outer segment tips; ROST, rod photoreceptor outer segment tips.

within the RPE cells into consideration⁴⁴ as follows. The contribution from the RPE cell layer can be decomposed into two components: (1) single scattering with no depolarization and (2) multiple scattering caused by melanin granules that exhibit depolarization. Because multiple scattering naturally elongates the optical path length, the corresponding profiles in the intensity and DOPU exhibit wide distributions [cf. in Ref. 44, a wide (fuzzy) distribution of intensity image in a healthy retina disappears in an albino retina, suggesting the contribution of the melanin granules in the RPE cells). With regard to the depolarization, the contribution from multiple scattering, which causes depolarization, appears in deeper locations than that from single scattering, and this leads to the displacement of the intensity peak and the DOPU minimum.

As a result, in the depolarizing material segmentation, the segmented pixels are at the depth position of the RPE cell layer located above the BM (sub-band denoted by *) and the position below the BM (sub-band denoted by **), while there are fewer segmented pixels in the middle of the thick band at the depth of BM, leading to a seemingly double-layered distribution of the RPE cells or its constituent pigments (melanin granules).

It should be stressed, however, from the aforementioned discussion, that this distribution does not exactly map the real position of the RPE cells or the pigments, but rather reflects echo-like tails originating from multiple scattering, i.e., the inner sub-band locates the RPE cells but at a slightly reduced thickness (the inner side is eroded) due to the transition from single to multiple scattering, and the other sub-band below BM locates nothing but the echo.

Figure 14 is an enlarged comparison of the multiple-frame and single-frame processed RPE segmentation images, in which the estimated location of the RPE cell layer is highlighted by a yellow rectangle. This suggests that the segmented pixels of the depolarizing material for RPE need to be interpreted as the segmented layer is thickened and approximately doubled in depth, so the outer half would be an artifact by echo, and most of the inner part is eroded. These differences between the segmentation results and the real distribution of the RPE cells would depend not only on the imaging and processing conditions, but also on the retina itself, especially in the case of patient eye imaging where RPE and its constituents would

undergo pathologic changes; therefore, the interpretation should be made with caution.

Another aspect is that *in vivo* retinal OCT imaging is always accompanied by speckles. As a result of this study, the effect of speckles leads to in-plane fluctuation of the fragmentations and breaks at the depth of BM in the thick band or the double-layered structure. At pixels where a speckle causes a weak signal from multiple scattering by RPE cells and a strong signal from BM, it results in a higher DOPU value, and vice versa. These fluctuations appear as the scattered red-orange spots at BM depth in Figs. 3(a), 4(a), 4(i), and 13(c). As an advantage of the high-resolution depolarization imaging by this small DOPU evaluation window, those scattered spots can be noticed as a speckle fluctuation.

In the lower-resolution conditions, e.g., segmentation by an 8×10 pixel DOPU evaluation window in single-frame image, this fluctuation appears differently. Figure 15 is a comparison with the single-frame processed image. In the single-frame image [Fig. 15(a)], the breaks appear as a complete loss of the RPE in those locations, whereas in the images from multiple frames [Figs. 15(b) and 15(c)], the double-layered structures can still be perceived and can be recognized as laterally continuous, indicating no RPE loss, although fluctuations are present. In order to interpret these results appropriately, corresponding DOPU images are also shown side-by-side in Figs. 15(d)–15(f). It can be observed that the red-orange spots in Figs. 15(e) and 15(f) are smeared out into the yellow areas in Fig. 15(d), which appear as a relatively large vacancy of RPE in the segmentation image [Fig. 15(a)]. Compared with the DOPU evaluation window size [magenta-colored rectangle in Figs. 15(a) and 15(c)], this smearing is probably caused by the low-pass filtering effect of the window. Considering that this retina is normal, the apparent RPE loss observed in Fig. 15(a) is likely an artifact; hence, a reasonable precaution from this example is that when interpreting the single-frame image with RPE breaks, one should think about the possibility of speckle artifacts, which could mimic real losses of RPE. Adaptation of the DOPU threshold might improve the results obtained by single-frame imaging.

As a conclusion, this high-resolution depolarization imaging by the smallest DOPU evaluation window with multiple-frame

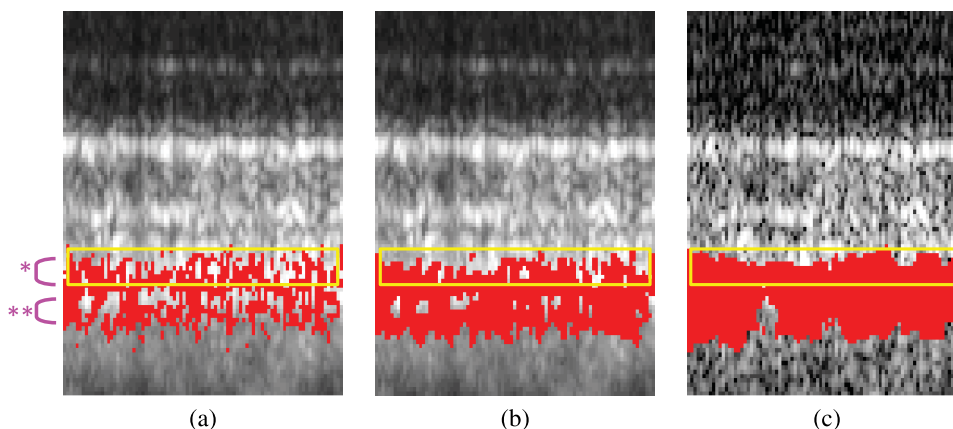


Fig. 14 RPE cell layer position estimated in depolarizing material segmentation overlaid on intensity images in healthy eye 1. (a) 50 frames processed by 1×1 (x, z) window. (b) 50 frames processed by 2×3 (x, z) window. (c) Single frame processed by 10×8 (x, z) window. Magenta brackets indicate depth ranges of the double layer. *Inner layer above Bruch's membrane, and **outer layer below Bruch's membrane. Yellow rectangles show estimated location of RPE cell layer.

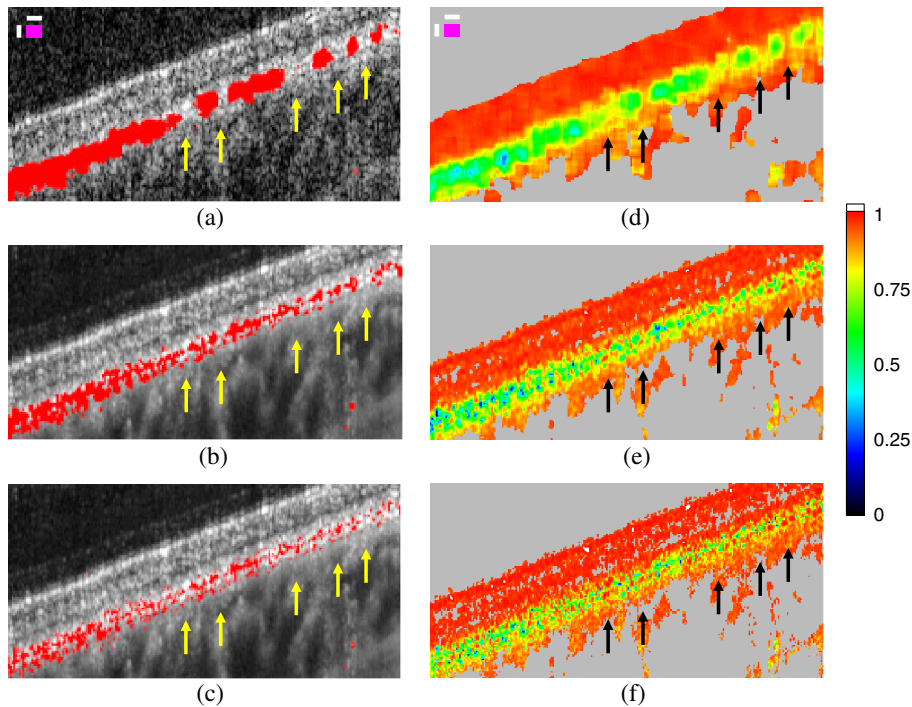


Fig. 15 (a) to (c) In-plane fluctuations of segmented depolarizing material (red pixels) overlaid on intensity images in healthy eye 3, accompanied by (d) to (f) the corresponding DOPU images. (a) and (d) Single frame processed with 10×8 (x, z) window. (b) and (e) 50 frames processed with 2×3 (x, z) window. (c) and (f) 50 frames processed with 1×1 (x, z) window, corresponding to Figs. 4(p) and 4(l), 4(n) and 4(j), 4(m) and 4(i). Yellow and black arrows indicate positions of breaks of segmented depolarizing material. In (a) and (c), white scale bars are 10 pixels (x , horizontal) and 8 pixels (z , vertical), and magenta rectangle indicates size of 10×8 (x, z) window.

processing would be beneficial for avoidance of inaccurate interpretations of RPE segmentation and for leading to an appropriate use of this depolarization imaging technique in research and clinical situations.

5 Conclusion

Using a PS-OCT system with an integrated tracker, we have demonstrated and investigated the impact of DOPU evaluation window size in 3-D for *in vivo* retinal PS-OCT imaging.

Optimum conditions for DOPU imaging and depolarizing tissue segmentation are discussed and proposed depending on practical criteria. By introducing a primary parameter, the 3-D DOPU evaluation window size in units of ORV of the imaging system, the figures of merit—sensitivity, efficiency, and susceptibility—were consistently analyzed. Interpretation of the DOPU and RPE segmentation images with a high resolution obtained by the smallest DOPU evaluation window was given, indicating the real positions of the RPE cell layer and BM within the broad hyper-reflective band of the RPE–BM complex, and the existence of a tailed artifact caused by multiple scattering.

The new findings and understandings of the optimum condition and the interpretation will lead to more accurate and robust use of depolarization imaging by PS-OCT in clinical imaging and studies.

References

1. M. R. Hee et al., "Polarization-sensitive low-coherence reflectometer for birefringence characterization and ranging," *J. Opt. Soc. Am. B* **9**(6), 903 (1992).
2. J. F. de Boer et al., "Two-dimensional birefringence imaging in biological tissue by polarization-sensitive optical coherence tomography," *Opt. Lett.* **22**(12), 934–936 (1997).
3. J. F. de Boer et al., "Imaging thermally damaged tissue by polarization sensitive optical coherence tomography," *Opt. Express* **3**(6), 212–218 (1998).
4. J. F. de Boer, T. E. Milner, and J. S. Nelson, "Determination of the depth-resolved Stokes parameters of light backscattered from turbid media by use of polarization-sensitive optical coherence tomography," *Opt. Lett.* **24**(5), 300–302 (1999).
5. C. Hitzenberger et al., "Measurement and imaging of birefringence and optic axis orientation by phase resolved polarization sensitive optical coherence tomography," *Opt. Express* **9**(13), 780–790 (2001).
6. J. F. de Boer and T. E. Milner, "Review of polarization sensitive optical coherence tomography and Stokes vector determination," *J. Biomed. Opt.* **7**(3), 359–371 (2002).
7. Y. Yasuno et al., "Birefringence imaging of human skin by polarization-sensitive spectral interferometric optical coherence tomography," *Opt. Lett.* **27**(20), 1803–1805 (2002).
8. D. Stifter et al., "Polarisation-sensitive optical coherence tomography for material characterisation and strain-field mapping," *Appl. Phys. A Mater. Sci. Process.* **76**(6), 947–951 (2003).
9. M. Góra et al., "Optical coherence tomography for examination of parchment degradation," *Laser Chem.* **2006**, 1–6 (2006).
10. M. Yamanari, S. Makita, and Y. Yasuno, "Polarization-sensitive swept-source optical coherence tomography with continuous source polarization modulation," *Opt. Express* **16**(8), 5892–5906 (2008).
11. D. Stifter, "Beyond biomedicine: a review of alternative applications and developments for optical coherence tomography," *Appl. Phys. B* **88**(3), 337–357 (2007).
12. W. Drexler and J. G. Fujimoto, "State-of-the-art retinal optical coherence tomography," *Prog. Retin. Eye Res.* **27**(1), 45–88 (2008).
13. B. Cense et al., "In vivo depth-resolved birefringence measurements of the human retinal nerve fiber layer by polarization-sensitive optical coherence tomography," *Opt. Lett.* **27**(18), 1610–1612 (2002).

14. M. Pircher et al., "Imaging of polarization properties of human retina in vivo with phase resolved transversal PS-OCT," *Opt. Express* **12**(24), 5940–5951 (2004).
15. M. Pircher et al., "Human macula investigated in vivo with polarization-sensitive optical coherence tomography," *Invest. Ophthalmol. Vis. Sci.* **47**(12), 5487–5494 (2006).
16. E. Götzinger et al., "Retinal pigment epithelium segmentation by polarization sensitive optical coherence tomography," *Opt. Express* **16**(21), 16410–16422 (2008).
17. Y. Yasuno et al., "Visibility of trabecular meshwork by standard and polarization-sensitive optical coherence tomography," *J. Biomed. Opt.* **15**(6), 061705 (2010).
18. B. Baumann et al., "Segmentation and quantification of retinal lesions in age-related macular degeneration using polarization-sensitive optical coherence tomography," *J. Biomed. Opt.* **15**(6), 061704 (2010).
19. M. Pircher, C. K. Hitzenberger, and U. Schmidt-Erfurth, "Polarization sensitive optical coherence tomography in the human eye," *Prog. Retin. Eye Res.* **30**(6), 431–451 (2011).
20. S. Zotter et al., "Large-field high-speed polarization sensitive spectral domain OCT and its applications in ophthalmology," *Biomed. Opt. Express* **3**(11), 2720–2732 (2012).
21. T. Torzicky et al., "Automated measurement of choroidal thickness in the human eye by polarization sensitive optical coherence tomography," *Opt. Express* **20**(7), 7564–7574 (2012).
22. B. Cense et al., "Thickness and birefringence of healthy retinal nerve fiber layer tissue measured with polarization-sensitive optical coherence tomography," *Invest. Ophthalmol. Vis. Sci.* **45**(8), 2606–2612 (2004).
23. M. Yamanari et al., "Phase retardation measurement of retinal nerve fiber layer by polarization-sensitive spectral-domain optical coherence tomography and scanning laser polarimetry," *J. Biomed. Opt.* **13**(1), 014013 (2008).
24. S. Zotter et al., "Measuring retinal nerve fiber layer birefringence, retardation, and thickness using wide-field, high-speed polarization sensitive spectral domain OCT," *Invest. Ophthalmol. Vis. Sci.* **54**(1), 72–84 (2013).
25. J. Lammer et al., "Detection and analysis of hard exudates by polarization-sensitive optical coherence tomography in patients with diabetic maculopathy," *Invest. Ophthalmol. Vis. Sci.* **55**(3), 1564–1571 (2014).
26. S. Michels et al., "Value of polarisation-sensitive optical coherence tomography in diseases affecting the retinal pigment epithelium," *Br. J. Ophthalmol.* **92**(2), 204–209 (2008).
27. C. Ahlers et al., "Imaging of the retinal pigment epithelium in age-related macular degeneration using polarization-sensitive optical coherence tomography," *Invest. Ophthalmol. Vis. Sci.* **51**(4), 2149–2157 (2010).
28. F. G. Schlanitz et al., "Performance of automated drusen detection by polarization-sensitive optical coherence tomography," *Invest. Ophthalmol. Vis. Sci.* **52**(7), 4571–4579 (2011).
29. C. Schütze et al., "Lesion size detection in geographic atrophy by polarization-sensitive optical coherence tomography and correlation to conventional imaging techniques," *Invest. Ophthalmol. Vis. Sci.* **54**(1), 739–745 (2013).
30. J. Lammer et al., "Imaging retinal pigment epithelial proliferation secondary to PASCAL photocoagulation *in vivo* by polarization-sensitive optical coherence tomography," *Am. J. Ophthalmol.* **155**(6), 1058–1067 (2013).
31. E. Götzinger et al., "Speckle noise reduction in high speed polarization sensitive spectral domain optical coherence tomography," *Opt. Express* **19**(15), 14568–14585 (2011).
32. R. D. Ferguson et al., "Tracking optical coherence tomography," *Opt. Lett.* **29**(18), 2139–2141 (2004).
33. D. X. Hammer et al., "Advanced scanning methods with tracking optical coherence tomography," *Opt. Express* **13**(20), 2139–2141 (2005).
34. Heidelberg Engineering GmbH, "Spectralis™," <http://www.heidelbergengineering.com/international/products/spectralis/> (25 August 2014).
35. M. Fleckenstein et al., "High-resolution spectral domain-OCT imaging in geographic atrophy associated with age-related macular degeneration," *Invest. Ophthalmol. Vis. Sci.* **49**(9), 4137–4144 (2008).
36. M. Hangai et al., "Ultrahigh-resolution versus speckle noise-reduction in spectral-domain optical coherence tomography," *Opt. Express* **17**(5), 4221–4235 (2009).
37. K. V. Vienola et al., "Real-time eye motion compensation for OCT imaging with tracking SLO," *Biomed. Opt. Express* **3**(11), 2950–2963 (2012).
38. M. Sugita et al., "Motion artifact and speckle noise reduction in polarization sensitive optical coherence tomography by retinal tracking," *Biomed. Opt. Express* **5**(1), 106–122 (2014).
39. O. Tan et al., "Speckle reduction in swept source optical coherence tomography images with slow-axis averaging," *Proc. SPIE* **8213**, 82132Z (2012).
40. M. Szkulmowski et al., "Efficient reduction of speckle noise in optical coherence tomography," *Opt. Express* **20**(2), 1337–1359 (2012).
41. J. M. Schmitt, S. H. Xiang, and K. M. Yung, "Speckle in optical coherence tomography," *J. Biomed. Opt.* **4**(1), 95–105 (1999).
42. D. C. Adler, T. H. Ko, and J. G. Fujimoto, "Speckle reduction in optical coherence tomography images by use of a spatially adaptive wavelet filter," *Opt. Lett.* **29**(24), 2878–2880 (2004).
43. International Electrotechnical Commission, "Safety of laser products. Part 1: equipment classification and requirements," IEC 60825–1, 2nd ed. (2007).
44. B. Baumann et al., "Polarization sensitive optical coherence tomography of melanin provides intrinsic contrast based on depolarization," *Biomed. Opt. Express* **3**(7), 1670–1683 (2012).
45. R. Leitgeb, C. Hitzenberger, and A. Fercher, "Performance of Fourier domain vs. time domain optical coherence tomography," *Opt. Express* **11**(8), 889–894 (2003).
46. T. Bajraszewski et al., "Improved spectral optical coherence tomography using optical frequency comb," *Opt. Express* **16**(6), 4163–4176 (2008).
47. M. Born and E. Wolf, *Principles of Optics—Electromagnetic Theory of Propagation, Interference and Diffraction of Light*, 7th ed., Cambridge University Press, Cambridge (1999).
48. V. V. Tuchin, L. Wang, and D. A. Zimnyakov, *Optical Polarization in Biomedical Applications*, Springer, Berlin Heidelberg (2006).
49. A. Hohmann et al., "Multiple scattering of polarized light: influence of absorption," *Phys. Med. Biol.* **59**(11), 2583–2597 (2014).
50. A. F. Fercher et al., "Optical coherence tomography—principles and applications," *Rep. Prog. Phys.* **66**, 239–303 (2003).
51. M. Hughes, M. Spring, and A. Podoleanu, "Speckle noise reduction in optical coherence tomography of paint layers," *Appl. Opt.* **49**(1), 99–107 (2010).
52. J. Baxi et al., "Retina-simulating phantom for optical coherence tomography," *J. Biomed. Opt.* **19**(2), 021106 (2014).
53. D. R. Williams, "Imaging single cells in the living retina," *Vis. Res.* **51**(13), 1379–1396 (2011).
54. J. S. Werner et al., "Outer retinal abnormalities associated with inner retinal pathology in nonglaucomatous and glaucomatous optic neuropathies," *Eye* **25**(3), 279–289 (2011).
55. C. Curcio and M. Johnson, "Structure, function, and pathology of Bruch's membrane," in *Retina*, S. J. Ryan et al., Eds., Vol. 1, 5th ed., pp. 466–481, Saunders/Elsevier, London, New York (2013).

Biographies of the authors are not available.